Journal of The Electrochemical Society

The Electrochemical Society
Advancing solid state & electrochemical science & technology

OPEN ACCESS

Printable Two-Dimensional V_2O_5/MXene Heterostructure Cathode for Lithium-Ion Battery

Journal of The Electrochemical Society, 2021 **168** 020507

Printable Two-Dimensional V_2O_5/MXene Heterostructure Cathode for Lithium-Ion Battery

Yang Wang,[1] Ties Lubbers,[1] Rui Xia,[1] Yi-Zhou Zhang,[2] Mohammad Mehrali,[1] Mark Huijben,[1] and Johan E. ten Elshof[1,z]

[1] *University of Twente, MESA+ Institute for Nanotechnology, 7500AE Enschede, the Netherlands*
[2] *Institute of Advanced Materials and Flexible Electronics (IAMFE), School of Chemistry and Materials Science, Nanjing University of Information Science & Technology, 210044, Nanjing, People's Republic of China*

Two-dimensional nanosheets show promise as electrode materials for high electrochemical performance lithium-ion batteries owing to their unique properties. However, individual nanosheets cannot meet all the required properties for batteries in one material to achieve optimal performance. Here, we demonstrate a new type of two-dimensional heterostructure cathode material for lithium-ion batteries by inkjet printing a composite ink based on high capacity V_2O_5 nanosheets and high electronic conductivity $Ti_3C_2T_x$ nanosheets. The excellent electronic conductivity of $Ti_3C_2T_x$ nanosheets and layer-by-layer heterostructure design enable fast electron transport and minimization of detrimental volume changes during the electrochemical process, respectively. The printed cathodes exhibit a high capacity of 321 mAh g^{-1} at 1C, high-rate capability of 112 mAh g^{-1} at 10.5C and good cycling stability after 680 cycles with 91.8% capacity retention, indicating high electrochemical performance of the printed heterostructure cathode. This work opens new opportunities of two-dimensional heterostructures for high performance energy storage applications.
 [DOI: 10.1149/1945-7111/abdef2]

Manuscript submitted November 3, 2020; revised manuscript received January 19, 2021. Published February 2, 2021.

Supplementary material for this article is available online

Development of new electrode materials are a challenge to the fabrication of high performance lithium-ion batteries (LIBs).[1,2] Two-dimensional (2D) materials have recently attracted considerable attention because of their distinct electronic properties, shortened ion diffusion paths and cycling stability for energy storage applications like lithium-ion batteries.[3] In particular, 2D materials exhibit enhanced electrochemical properties because of the increased number of surface active sites and surface area.[4] A wide range of 2D materials such as graphene,[5] transition metal dichalcogenides[6] and transition metal oxides[7] have been demonstrated as promising electrode materials for LIBs. Among them, 2D vanadium pentoxide (V_2O_5) nanosheets show great promise as a cathode material for LIBs because of their high theoretical capacity of 294.8 mAh g^{-1} with two lithium ion intercalations per unit cell in its structure for a potential window between 2 and 4 V.[8] However, the intrinsic poor electronic conductivity of V_2O_5 nanosheets limits the electrochemical performance. Therefore, individual 2D nanosheets cannot meet all properties to maximize battery electrochemical performance such as energy/power density and cycle life. 2D nanosheets exhibit various interesting electronic properties like metallic conductivity, semiconductivity or insulating behavior.[9] We argue that fabricating heterostructure electrodes by stacking different types of 2D nanosheets will open up new opportunities to realize high electrochemical performance electrodes by combining the advantages of different 2D nanosheet building blocks while eliminating their limitations.[10] For instance, combining high theoretical capacity nanosheet materials with metallic conductivity nanosheets into 2D heterostructure may result in synergistic enhancement of electrochemical properties. More generally, 2D heterostructures with multiple active sites and large interlayer distance not only show the capability to accommodate large electrolyte ions and decrease energy barriers for electrolyte ion diffusion, but also enhance the specific capacity and energy density by incorporating large numbers of ions into electrodes. 2D heterostructures with excellent electronic conductivity enables fast electron transport, resulting in power density enhancement. Moreover, 2D heterostructures show high capability to accommodate large mechanical stresses and strains during ion intercalation and de-intercalation processes, resulting in long cycle life. Lastly, 2D heterostructures with tunable properties can be achieved by surface terminations through atomic engineering.

MXene is a new class of 2D materials with the general formula $M_{n+1}X_nT_x$, where M is an early transition metal, X is C or N, T_x is a surface termination functional group such as –OH, –O or –F, and n = 1, 2, 3, 4.[11] MXene nanosheets that exhibit excellent electronic conductivity, high specific surface area and hydrophilicity show promise as charge transport materials.[12] Moreover, water-based MXene nanosheet suspensions can be used as inks for versatile, digital and low-cost inkjet printing.[12] Printed electronics exhibit potential for low-cost, flexible and high-performance electronics devices.[13,14] Among them, inkjet printing shows promise for the fabrication of electrodes with controlled thickness, roughness, and interface for lithium-ion batteries. Realizing controllable interface for printed heterostructures is crucial for high performance electrodes.

$Ti_3C_2T_x$ nanosheets, which have been widely studied, are used in this work. Here we show a versatile method for the fabrication of a thin-film heterostructure cathode by inkjet printing a water-based V_2O_5/$Ti_3C_2T_x$ nanosheet composite ink. The novel printed heterostructure cathode provide more active sites for charge storage during electrochemical measurements, resulting in a high capacity.

Experimental

Synthesis of V_2O_5 nanosheets.—In order to synthesize V_2O_5 nanosheets, VO_2 (B) nanosheets were first prepared from a V_2O_5 powder by hydrothermal reaction, as described elsewhere,[15] followed by oxidation into V_2O_5 nanosheets by thermal annealing in air. The reaction mixture (10 mL) was prepared by dispersing 20 mg V_2O_5 powder (Alfa Aesar >99.6%) in 2 mL deionized (DI) water by ultrasonication treatment for 5 min. Then, 4 mL H_2O_2 (Sigma 30% in H_2O) was added whilst stirring vigorously. The dispersion was stirred for another 5 min resulting in a clear yellow solution. 4 mL isopropyl alcohol (IPA, Boom, technical grade) was added and stirred for another 5 min. The addition of IPA was accompanied by mild oxygen bubbling, which was generated from the solution. Then, a certain amount of reaction mixture was placed in an autoclave reactor vessel which was then heated to 180 °C for 6 h. The reacted suspension was washed with ethanol three times by centrifuging for 10 min at 8000 rpm. The collected dark blue precipitate was then re-

[z] E-mail: j.e.tenelshof@utwente.nl

dispersed in DI water by ultrasonication for one hour to make sure that all individual nanostructures were separated as good as possible. The suspension was then filtered on a flat filter paper using vacuum filtration. The filter paper with materials was dried in an oven at 80 °C for at least 2 h to obtain dried VO_2 (B) nanosheets. The dried VO_2 (B) nanosheet film was peeled off and then calcined in a tube oven for 2 h at 350 °C with a heating ramp rate of 2 °C min^{-1} to convert into V_2O_5 nanosheets.

Synthesis of $Ti_3C_2T_x$ nanosheets.—Titanium carbide ($Ti_3C_2T_x$) MXene was prepared similar to a previously reported method.[16] Typically, the etchant solution was prepared by dissolving 3.2 g of lithium fluoride (LiF, Sigma-Aldrich, −300 mesh powder, 98.5%) into 40 mL of 9 M HCl (Sigma-Aldrich, 37% solution in water). Subsequently, 2 g of Ti_3AlC_2 powder (400 mesh) was added into the etchant solution over the course of 10 min and kept the reaction temperature was at 35 °C. After reaction for 24 h, the resultant was washed with DI water repeatedly and delaminated manually by hand shaking agitation to obtain $Ti_3C_2T_x$ MXene suspension. The prepared solution was stored in a nitrogen-sealed vial and used as the MXene ink.

Inkjet printing.—The traditional method to fabricate V_2O_5 cathodes is by mixing V_2O_5 powder: conductive agent: binder in a mass ratio of 7: 2: 1. Therefore, a mass ratio of 8: 2 for V_2O_5: $Ti_3C_2T_x$ was used in this study. A printable ink was prepared by dispersing V_2O_5 nanosheets into a $Ti_3C_2T_x$ nanosheet suspension followed by ultrasonication to achieve a homogeneous suspension. All electrodes were inkjet printed onto oxygen plasma treated stainless steel foil substrates with a drop spacing of 20 μm at 30 °C by a Dimatix DMP-2800 inkjet printer (Fujifilm Dimatix), which was equipped with a 10 pL cartridge (DMC-11610). The printed electrodes were subsequently dried in a vacuum oven at 60 °C overnight.

Electrochemical characterization.—For electrochemical characterization the printed $V_2O_5/Ti_3C_2T_x$ cathode was assembled with a lithium metal anode and a glass fiber separator in an electrochemical EL-CELL in an argon atmosphere glovebox (<0.1 ppm of H_2O and O_2). 1 M $LiPF_6$ in 1:1 ethylene carbonate dimethyl carbonate (EC: DMC) was used as electrolyte. All electrochemical measurements were conducted at room temperature using a BioLogic VMP-300 system in a two-electrode setup. The cyclic voltammetry (CV) and galvanostatic charge/discharge experiments were performed between 2 and 4 V. Only the mass of active material of V_2O_5 was considered in the capacity calculations. Therefore, the current density of 1C is 294 mA g^{-1}.

For *ex situ* X-ray photoelectron spectroscopy (XPS) spectra, the LIBs were discharged and stopped at specific potentials related to the electrochemical reactions. The LIBs were then transferred into a glovebox for disassembly. The electrodes were rinsed with dimethyl carbonate (Aldrich, 99.9%) to remove excel electrolyte. Finally, the electrodes were transferred to an XPS chamber within a short time period.

Materials characterization.—X-ray diffraction (XRD) analysis was done with a PANalytical X'Pert Pro with filtered Cu Kα radiation (λ = 0.15405 nm). XPS spectra were recorded using an Omicron Nanotechnology GmbH (Oxford Instruments) surface analysis system with a photon energy of 1486.7 eV (Al Kα X-ray source) with a scanning step size of 0.1 eV. The pass energy was set to 20 eV. The spectra were corrected using the binding energy of C 1s of adventitious carbon as a reference. Atomic Force Microscopy (AFM) (Veeco Dimension Icon) was conducted in standard tapping mode. The AFM data were analyzed by Gwyddion (version 2.47) software. High resolution scanning electron microscopy (HRSEM; Zeiss MERLIN) was performed to acquire information of V_2O_5 nanosheets and printed $V_2O_5/Ti_3C_2T_x$ electrode.

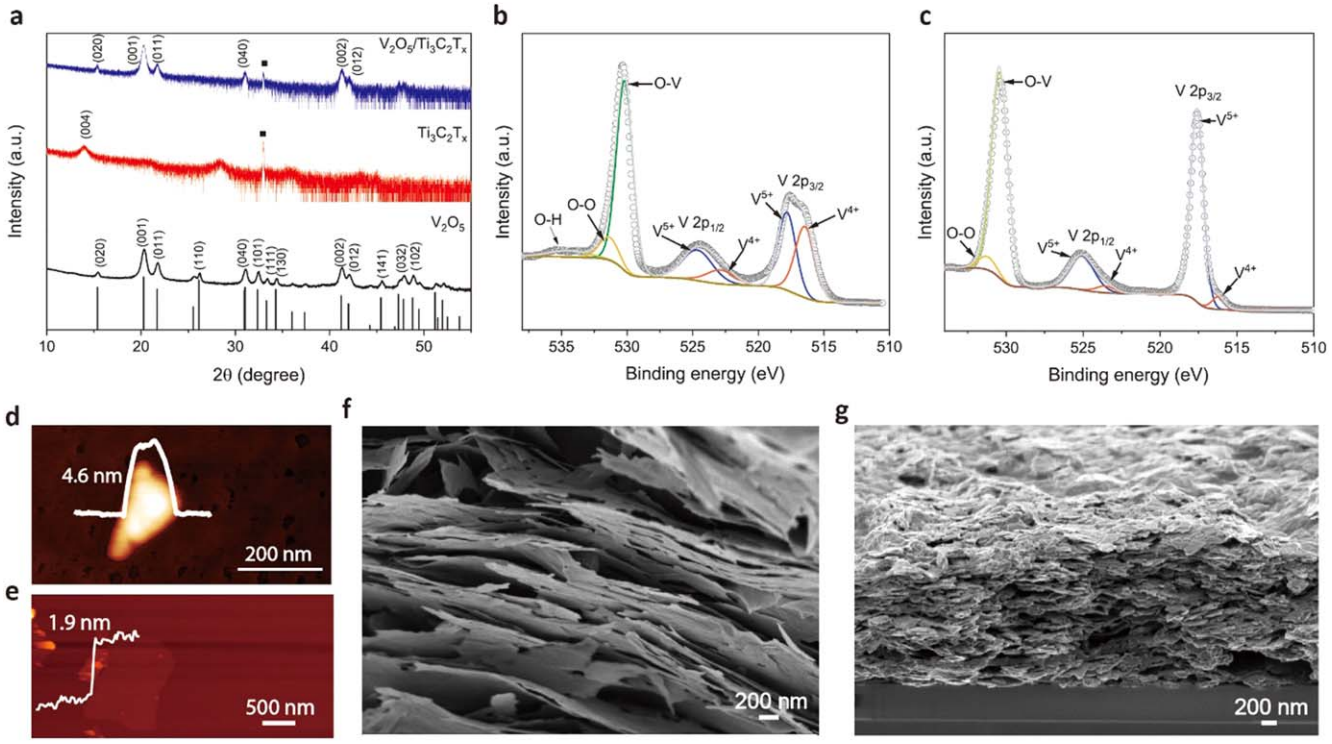

Figure 1. Materials characterization. (a) XRD patterns of 2D V_2O_5, $Ti_3C_2T_x$ and printed $V_2O_5/Ti_3C_2T_x$ film. The black symbols represent peaks from underlying silicon substrates. High-resolution XPS spectra of (b) VO_2 (B) and (c) V_2O_5 nanosheets. AFM images of (d) V_2O_5 nanosheet and (e) $Ti_3C_2T_x$ nanosheet. Cross-sectional SEM images of (f) vacuum filtrated V_2O_5 nanosheet film and (g) inkjet printed $V_2O_5/Ti_3C_2T_x$ film.

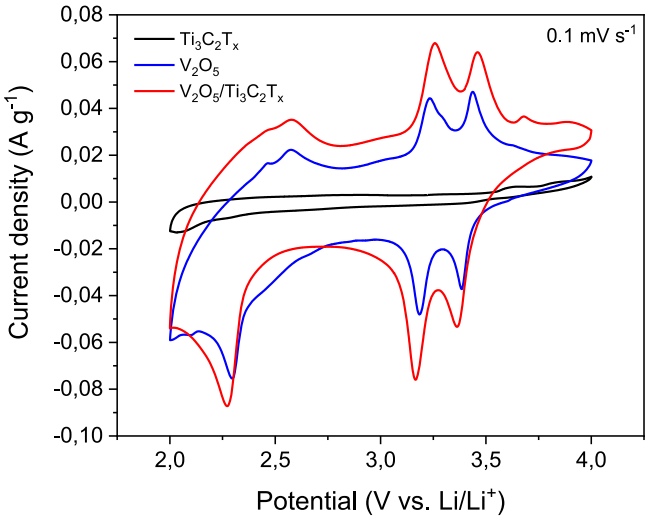

Figure 2. CV profiles of printed $V_2O_5/Ti_3C_2T_x$ cathode, printed V_2O_5 nanosheet cathode and printed $Ti_3C_2T_x$ electrode at a scan rate of 0.1 mV s^{-1} between 2 and 4 V in half-cells.

Results and Discussion

During the synthesis procedure the color of the V_2O_5 solution changed from orange to bright yellow after adding H_2O_2, indicating the formation of a V_2O_5 sol.[15,17] The addition of isopropanol into the solution was done to reduce V_2O_5 to VO_2 (B) species with a layered structure.[15] The VO_2 (B) nanosheets were thermally annealed at 350 °C in the air for 2 h to obtain V_2O_5 nanosheets. XRD analysis was performed to determine the crystal structure and phase information of the as-prepared VO_2 and V_2O_5 nanosheets. As shown in Fig. S1 (available online at stacks.iop.org/JES/168/020507/mmedia) (SI), the obtained VO_2 (B) nanosheets were in good accordance with monoclinic VO_2 (B) (JCPDS card no. 81–2392, space group *C*2/*m*, No. 12, $a = 12.05$ Å, $b = 3.70$ Å, $c = 6.41$ Å, $\beta = 106.86°$).[18] The reflections of the (00 *l*) series peaks indicate the lamellar and ultrathin features of the prepared sample. In particular, the (00*l*) series peaks have a high intensity compared to the other peaks, and the (010) peak is almost completely absent. The relative intensity change compared to the JCPDS card reference is probably due to alignment of the VO_2 (B) nanostructures.[15] The XRD pattern of the V_2O_5 nanosheets is shown in Fig. 1a. The spectrum is in good accordance with orthorhombic V_2O_5 (JCPDS card no. 74-4605, space group *Pmmn,* No. 59, $a = 11.46$ Å, $b = 4.36$ Å, $c = 3.57$ Å).[19] The (00 *l*) series reflections are relatively intense compared to the expected intensity described in the card. Examples of peaks with much lower intensities compared to the JCPDS card values are the (020) reflection at $2\theta = 15.5°$ and the (110) reflection at $2\theta = 26.2°$. The XRD diffractogram of printed $Ti_3C_2T_x$ film shows the (004) peak at $2\theta = 14.1°$ indicating a high degree of ordering in the *c* direction. For printed $V_2O_5/Ti_3C_2T_x$ heterostructure films, the (00*l*) peaks are pronounced suggesting a well-defined *c* orientation of the heterostructure electrode with stacked nanosheets. However, the presence of small (011), (040) and (012) peaks indicate that exfoliation of V_2O_5 nanosheets was not entirely completed. Moreover, $Ti_3C_2T_x$ nanosheets peaks are absent indicating that they are completely dispersed without aggregation.

The high-resolution XPS spectra were recorded to obtain oxidation state information on the prepared VO_2 (B) and V_2O_5 nanosheets. Figure 1b shows two binding energy (BE) peaks of vanadium in VO_2 (B), which can be assigned to V $2p_{3/2}$ and V $2p_{1/2}$, respectively. The BE of V $2p_{3/2}$ at 517.8 and 516.4 eV can be attributed to the V^{5+} and V^{4+} oxidation states, respectively. Note that VO_2 (B) is expected to have only V^{4+} while the XPS shows that the surface also contains V^{5+} in approximately a 50: 50% ratio. The presence of the V^{5+} component is probably due to the existence of V_2O_5 at the surface of VO_2 (B) resulting from exposure to air.[20] The high resolution spectrum of O 1*s* at 530.2, 531.4 and 534.5 eV corresponds to the presence of O-V, O-O and O-H groups, respectively. As shown in Fig. 1c, the main peak BE of V $2p_{3/2}$ at 517.6 eV and the small peak at 516.2 eV in V_2O_5 correspond to V^{5+} and V^{4+}, respectively.[21] The small amount of V^{4+} present in V_2O_5 samples could because of the photoreduction by the irradiation of V_2O_5 surface with the Al Kα X-rays during XPS measurement.[22] The BE difference between the O 1*s* and V $2p_{3/2}$ levels for the V^{5+} is 12.8 eV which identical to the reported value.[23] Similar to VO_2 (B), peaks in the high resolution spectrum of O 1*s* at 530.4 and 531.2 eV correspond to the O-V and O-O groups, respectively.

The thickness of V_2O_5 nanosheets was determined by AFM to be around 4.6 nm, which is in agreement with reported data, indicating an ultra-thin structure with several layers (Fig. 1d).[15] The thickness of the $Ti_3C_2T_x$ nanosheets is about 1.9 nm, suggesting an unilamellar structure (Fig. 1e). The thickness difference between the measured unilamellar $Ti_3C_2T_x$ nanosheets and the theoretical thickness, which is 0.98 nm, can be explained by the presence of molecular surface water.[24] The cross-sectional SEM image of a V_2O_5 nanosheet film (Fig. 1f) shows a high concentration of nanosheets present in lamellar structure, and even single sheets and agglomerated sheets can be distinguished. The prepared water-based $V_2O_5/Ti_3C_2T_x$ composite ink shows a high quality viscoelastic behavior which was confirmed by the optical images of droplet formation vs time as shown in Fig. S2 (SI). The cross-sectional SEM image of a printed $V_2O_5/Ti_3C_2T_x$ electrode on a silicon substrate shows a high degree of orientation with a layer-by-layer structure (Fig. 1g). The horizontal orientation of 2D heterostructures would facilitate electrolyte ion diffusion during the electrochemical process. Moreover, the printed electrode shows continuous coverage over a large area (Fig. S3, SI), indicating the reliability of inkjet printing to fabricate thin film electrodes.

The electrochemical performances of a printed $V_2O_5/Ti_3C_2T_x$ cathode, a printed V_2O_5 nanosheet cathode and a printed $Ti_3C_2T_x$ electrode were studied in half-cell configurations with lithium metal as anode. As shown in Fig. 2, the printed $Ti_3C_2T_x$ electrode shows only a small current response in the CV profile as compared to a $V_2O_5/Ti_3C_2T_x$ cathode at a scan rate of 0.1 mV s^{-1}, indicating that $Ti_3C_2T_x$ exhibits only a small contribution to the total current response. The $V_2O_5/Ti_3C_2T_x$ cathode exhibited a higher current density than the printed V_2O_5 nanosheets cathode, suggesting that the addition of $Ti_3C_2T_x$ nanosheets enhanced the charge transport. Moreover, the 1st to 4th CV curves of a printed V_2O_5 nanosheet cathode at a scan rate of 0.2 mV s^{-1} showed a current decrease for the redox peak at 2.3 V (Fig. S4, SI), while the CV curves of the printed $V_2O_5/Ti_3C_2T_x$ cathode almost overlapped at a scan rate of 0.2 mV s^{-1} (Fig. S5, SI), further indicating that the addition of $Ti_3C_2T_x$ nanosheets into V_2O_5 materials improved the cathode's electrochemical performance. The large current response of the printed $V_2O_5/Ti_3C_2T_x$ cathode originated mainly from the V_2O_5 nanosheets which show multiple redox peaks during lithium intercalation (about 3.4, 3.2, 2.3 V) and deintercalation (about 2.6, 3.3, 3.5 V) into V_2O_5 nanosheets, respectively.

Figure 3a shows the 1st to 4th cycle of the CV curves of a printed $V_2O_5/Ti_3C_2T_x$ cathode. Three anodic peaks corresponding to the first lithium ion deintercalation of γ/δ (peak 1), the second lithium ion deintercalation of δ/ε (peak 2) and ε/α (peak 3) phase transitions at equilibrium potential at around 2.6 V, 3.3 V and 3.5 V, respectively. The three cathodic peaks corresponding to the first lithium ion intercalation of α/ε (peak 6) and ε/δ (peak 5), the second lithium ion intercalation of δ/γ (peak 4) phase transitions at equilibrium potentials at around 3.4, 3.2 and 2.3 V, respectively.[8] The below reactions show the lithium ion intercalation steps:

$$\alpha - V_2O_5 + 0.5Li^+ + 0.5e^- \leftrightarrow \varepsilon\text{-}Li_{0.5}V_2O_5 \qquad [1]$$

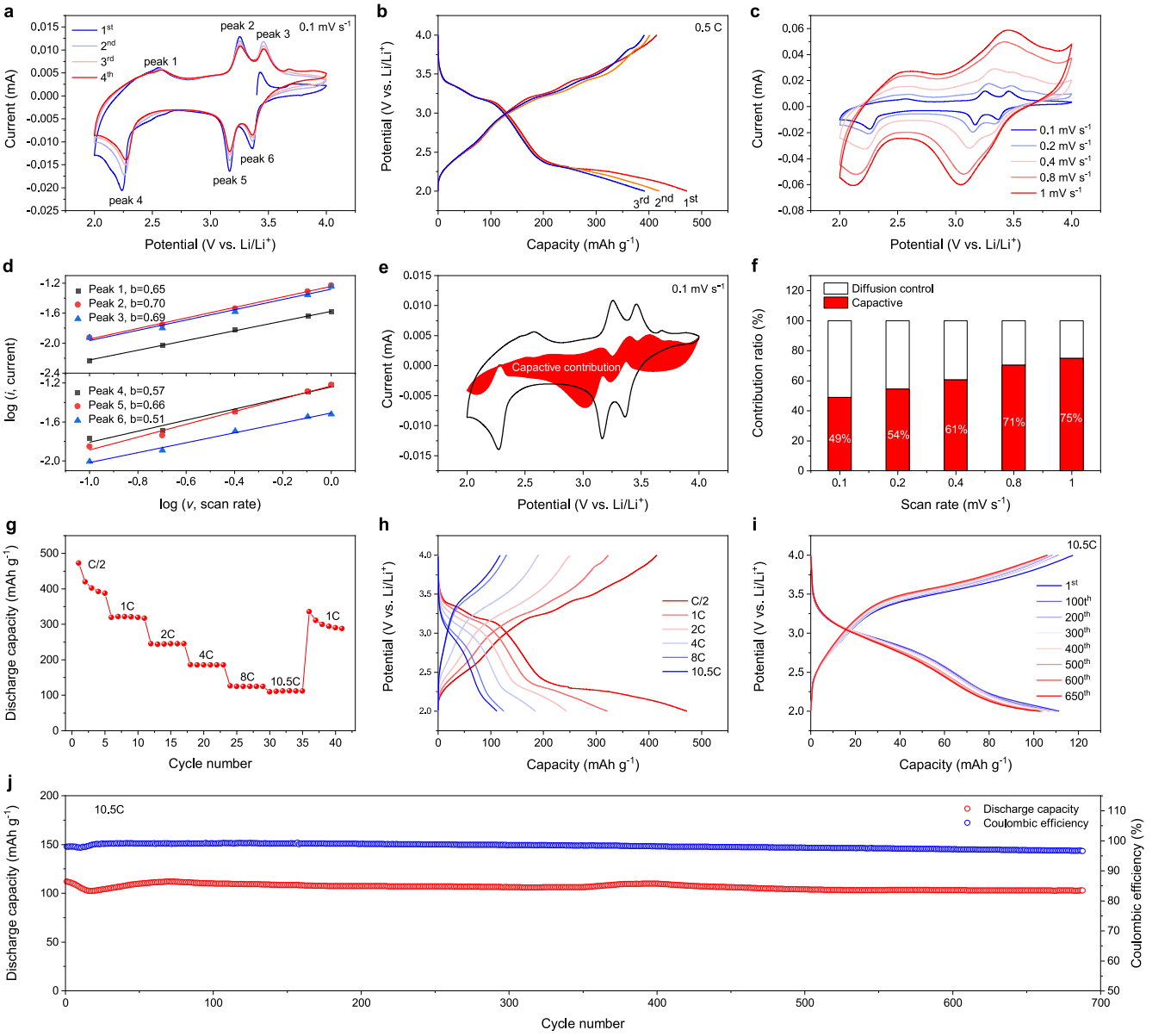

Figure 3. Electrochemical analysis of a printed $V_2O_5/Ti_3C_2T_x$ cathode in a half-cell. (a) First to fourth CV cycle at a scan rate of 0.1 mV s^{-1} between 2 and 4 V. (b) First to third cycle galvanostatic charge/discharge curves at 0.5C. (c) CV cycle of printed $V_2O_5/Ti_3C_2T_x$ cathodes from 0.1 to 1 mV s^{-1}. (d) The log(i) vs log (v) plot of the charge peaks (above) and discharge peaks (bottom). (e) k_1, k_2 analysis of printed $V_2O_5/Ti_3C_2T_x$ cathodes at 0.1 mV s^{-1}. The red area shows the contribution of surface capacitance as a function of potential. (f) The surface capacitive contribution and diffusion control ratio at different scan rates. (g) Discharge capacity of printed $V_2O_5/Ti_3C_2T_x$ cathodes at different discharge rates. (h) Galvanostatic charge/discharge curves of printed $V_2O_5/Ti_3C_2T_x$ cathodes at different discharge rates. (i), (j) Cycling performance of printed $V_2O_5/Ti_3C_2T_x$ cathodes at 10.5C.

$$\varepsilon - Li_{0.5}V_2O_5 + 0.5Li^+ + 0.5e^- \leftrightarrow \delta - LiV_2O_5 \quad [2]$$

$$\delta - LiV_2O_5 + Li^+ + e^- \leftrightarrow \gamma - Li_2V_2O_5 \quad [3]$$

It is noticeable that V_2O_5 nanosheets has multiple phase transitions during lithium ion intercalation/deintercalation, which coincide completely with the V_2O_5 bulk materials.[8] The peak current values decrease from the 1st to the 4th cycle, which could be because of solid electrolyte interface (SEI) layer formation. Galvanostatic charge/discharge curves also show the capacity decrease during the first to third cycles (Fig. 3b). Three plateaus were observed in discharge curves that correspond to the cathodic peaks in Fig. 3a. The subsequent 1st to 4th CV curves at a scan rate of 0.2 mV s^{-1} almost overlap, suggesting good cycling and stability after the first several cycles (Fig. S5, SI). An additional cathodic peak at around 3.6 V can be attributed to the irreversible phase transition of γ/γ' system.[25]

Kinetics analysis was performed to further explore the surface and bulk contributions to the electrochemical performance of printed $V_2O_5/Ti_3C_2T_x$ cathodes. Figure 3c shows the CV curves of printed $V_2O_5/Ti_3C_2T_x$ cathodes at scan rates from 0.1 to 1 mV s^{-1}. The surface capacitive effect can be determined by calculating the value of b through the relation of $i = av^b$ where i and v are the current and scan rate, a and b are adjustable parameters.[26] When the b value is close to 0.5, the electrochemical process is dominated by an ionic diffusion control mechanism. A b value close to 1 indicates a surface capacitive mechanism.[26] Figure 3d plots the log i vs log v linear relationships at their peak potentials. The b values of peaks 1, 2, 3, 4, 5, 6 are 0.65, 0.70, 0.69, 0.57, 0.66 and 0.51, respectively, suggesting synergistic contributions by both diffusion control and surface capacitive processes. Moreover, the current response i at

fixed potential (V) can be separated into surface capacitive (k_1v) and diffusion control mechanisms $k_2v^{1/2}$ using the equation $i(V) = k_1v + k_2v^{1/2}$.[26,27] Figure 3e shows the surface capacitive current (red region), compared with the total current in the CV profile at scan rate of 0.1 mV s^{-1}. The surface capacitive processes contribute almost half of the total current. It is noticeable that the calculated surface capacitive contribution is out of the range of the total CV curve in several parts, which could be explained by considering that the calculated surface capacitive contribution from CV curves is an ideal calculation. The dynamic resistance in a real electrochemical process could lead to hysteresis in the current response.[28] Furthermore, the surface capacitive contributions increase to 75% when the scan rate increases to 1 mV s^{-1}, suggesting that the surface capacitive dominates the electrochemical process at high scan rates, which is beneficial for rate performance (Fig. 3f).

Moreover, the printed $V_2O_5/Ti_3C_2T_x$ cathodes show good rate performance, as shown in Fig. 3g. After an initial capacity decrease in the first five cycles, possibly because of SEI layer formation, stable capacities of 321, 245, 185, 124 and 112 mAh g^{-1} were achieved at 1, 2, 4, 8 and 10.5C, respectively. More importantly, a high capacity of 112 mAh g^{-1} was achieved even at high C rate of 10.5C with high capacity retention of 65.7% compared to 321 mAh g^{-1} at 1C, indicating the high rate performance of the printed $V_2O_5/Ti_3C_2T_x$ electrode. The corresponding individual galvanostatic charge/discharge curves are shown in Fig. 3h. Three plateaus are visible at around 3.3, 3.2 and 2.3 V for discharge curves, corresponding to peaks 6, 5 and 4 in the CV curves (Fig. 3a). Cycling performance was conducted at 10.5C as shown in Figs. 3i–3j. The half-cell showed still good stable performance after around 680 cycles with a capacity retention of 91.7% and a coulombic efficiency of 96.5%.

As shown in Fig. 4, the average capacity fading rate is about 0.01% per cycle which is lower than other previously reported V_2O_5-based cathodes (Table SI, SI).[25,29–37] Moreover, printed $V_2O_5/Ti_3C_2T_x$ cathodes exhibit a capacity as high as 112 mAh g^{-1} at current density as high as 3000 mA g^{-1}. The excellent rate and cycling performances of the printed $V_2O_5/Ti_3C_2T_x$ cathode are beneficial from following aspects: the large specific surface area of 2D V_2O_5 nanosheets facilitates lithium ion diffusion during intercalation and deintercalation; the high surface capacitive contribution enables high capacity at high scan rate; the excellent electronic conductivity of the $Ti_3C_2T_x$ nanosheets in the heterostructure electrodes enables good electron transport; and the layer-by-layer heterostructure of printed nanosheets cathode minimizes the volume change within the cathode during charging and discharging processes.

Ex situ XPS spectra were recorded to analyze how the oxidation state of vanadium changes in printed $V_2O_5/Ti_3C_2T_x$ cathodes during the discharge process. As shown in Fig. 5, the pristine V $2p_{3/2}$ spectrum shape shows a strong V^{5+} peak and a small amount of V^{4+}. When the LIB was discharged to 3.4 V, the XPS spectrum of V $2p$ could be deconvoluted into two spin–orbit doublets which are V^{4+} and V^{5+}, indicating the oxidation state change of vanadium upon Li ion intercalation. It is noted that the V^{4+} peak has a comparable intensity as V^{5+} at 3.4 V. The amount of V^{4+} increases further when discharged to 3.2 V, suggesting further Li ion intercalation. When discharged to 2.3 V, the amount of V^{4+} is much larger than that of V^{5+}, indicating Li ion intercalations at 2.3 V. Therefore, the *ex situ* XPS spectra confirm the Li ion intercalation processes by analyzing the oxidation state of vanadium in printed $V_2O_5/Ti_3C_2T_x$ cathodes at different discharge plateaus.

Conclusions

A water-based 2D $V_2O_5/Ti_3C_2T_x$ composite ink was inkjet printed to fabricate heterostructures cathodes for LIBs. The printed cathode was composed of a layer-by-layer structure, combining the advantageous characteristics of high theoretical capacity V_2O_5 and high electrical conductivity $Ti_3C_2T_x$ nanosheets, exhibiting capacity

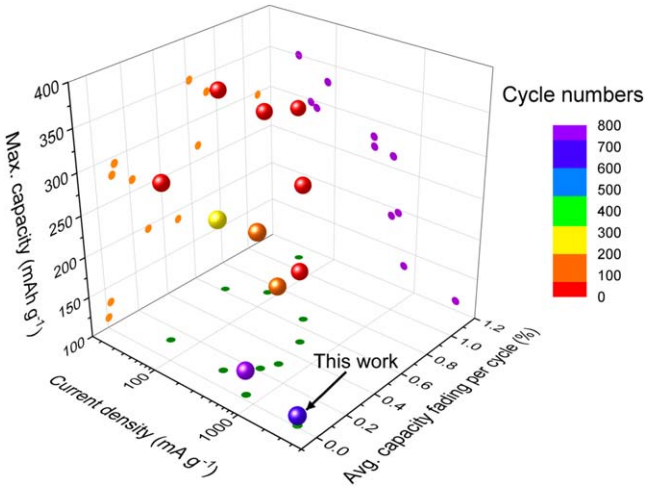

Figure 4. Comparison of the electrochemical performance of printed $V_2O_5/Ti_3C_2T_x$ cathodes and V_2O_5-based composite cathodes illustrated by 3D scatter bubble plots of maximum capacity (mAh g^{-1}), measured current density (mA g^{-1}) and average capacity fading per cycle (%). The colors of the bubbles show the cycle numbers.

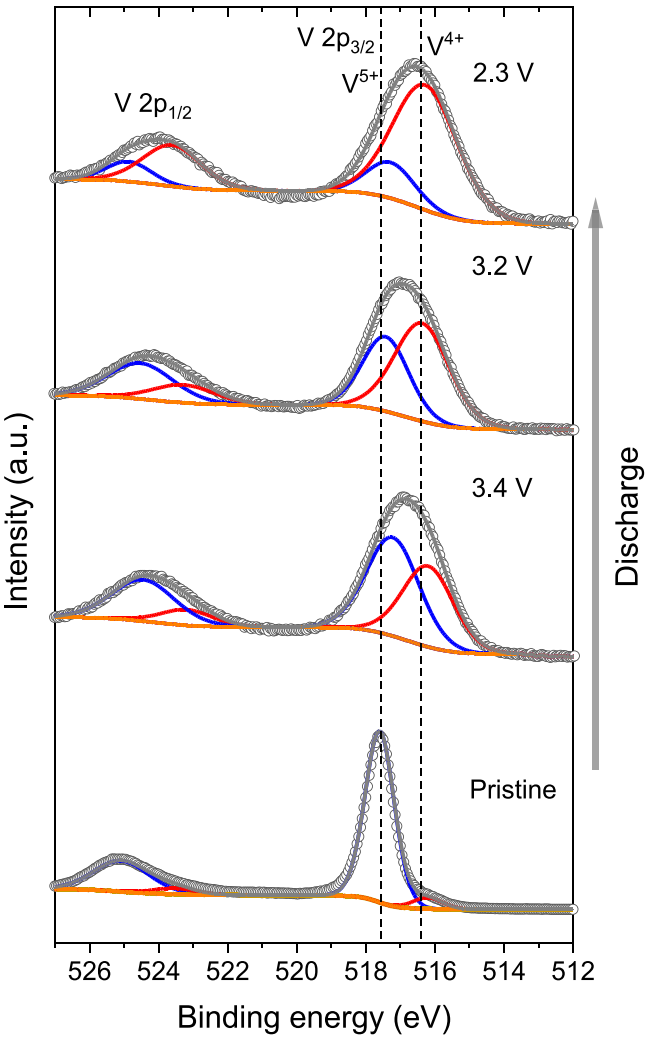

Figure 5. *Ex situ* XPS spectra of V $2p$ collected at different discharge plateaus in LIBs. The dashed lines indicate different oxidation states of vanadium.

as high as 321 mAh g^{-1} at 1C and long cycling stability when operated as a LIB. Therefore, inkjet printed two-dimensional heterostructure-based electrodes which combine advantages and elimination the limitations of individual 2D materials, open a new opportunity to high electrochemical performance batteries.

Acknowledgments

Y.W. and R.X. acknowledges the financial support of the China Scholarships Council program (CSC, No. 201608340058 and 201807720013, respectively). M. Smithers is acknowledged for performing the HR-SEM experiments.

ORCID

Yang Wang https://orcid.org/0000-0003-0113-1830
Johan E. ten Elshof https://orcid.org/0000-0001-7995-6571

References

1. S. Wang, L. Zhang, Q. H. Zeng, X. Liu, W. Y. Lai, and L. Y. Zhang, *ACS Sustain. Chem. Eng.*, **8**, 3200 (2020).
2. S. Wang, L. Zhang, J. Li, Q. Zeng, X. Liu, P. Chen, W.-Y. Lai, T. Zhao, and L. Zhang, *Electrochim. Acta*, **320**, 134560 (2019).
3. E. Pomerantseva, F. Bonaccorso, X. Feng, Y. Cui, and Y. Gogotsi, *Science*, **366**, eaan8285 (2019).
4. L. Peng, Y. Zhu, D. Chen, R. S. Ruoff, and G. Yu, *Adv. Energy Mater.*, **6**, 1600025 (2016).
5. M. F. El-Kady, Y. Shao, and R. B. Kaner, *Nat. Rev. Mater.*, **1**, 16033 (2016).
6. M. Chhowalla, H. S. Shin, G. Eda, L.-J. Li, K. P. Loh, and H. Zhang, *Nat. Chem.*, **5**, 263 (2013).
7. P. He, H. Yu, D. Li, and H. Zhou, *J. Mater. Chem.*, **22**, 3680 (2012).
8. Y. Yue and H. Liang, *Adv. Energy Mater.*, **7**, 1602545 (2017).
9. H. Zhang, *ACS Nano*, **9**, 9451 (2015).
10. E. Pomerantseva and Y. Gogotsi, *Nat. Energy*, **2**17089 (2017).
11. B. Anasori, M. R. Lukatskaya, and Y. Gogotsi, *Nat. Rev. Mater.*, **2**, 16098 (2017).
12. Y. Z. Zhang, Y. Wang, Q. Jiang, J. K. El-Demellawi, H. Kim, and H. N. Alshareef, *Adv. Mater.*, **32**, e1908486 (2020).
13. Y. Z. Zhang, Y. Wang, T. Cheng, L. Q. Yao, X. Li, W. Y. Lai, and W. Huang, *Chem. Soc. Rev.*, **48**, 3229 (2019).
14. D. Li, W. Y. Lai, Y. Z. Zhang, and W. Huang, *Adv. Mater.*, **30**, 1704738 (2018).
15. S. Liang, Y. Hu, Z. Nie, H. Huang, T. Chen, A. Pan, and G. Cao, *Nano Energy*, **13**, 58 (2015).
16. J. D. Cain, A. Azizi, K. Maleski, B. Anasori, E. C. Glazer, P. Y. Kim, Y. Gogotsi, B. A. Helms, T. P. Russell, and A. Zettl, *ACS Nano*, **13**, 12385 (2019).
17. C. J. Fontenot, J. W. Wiench, M. Pruski, and G. L. Schrader, *J. Phys. Chem. B*, **104**, 11622 (2000).
18. Y. Oka, T. Yao, N. Yamamoto, Y. Ueda, and A. Hayashi, *J. Solid State Chem.*, **105**, 271 (1993).
19. R. Enjalbert and J. Galy, *Acta Crystallogr. C*, **42**, 1467 (1986).
20. F. Ureña-Begara, A. Crunteanu, and J.-P. Raskin, *Appl. Surf. Sci.*, **403**, 717 (2017).
21. G. Silversmit, D. Depla, H. Poelman, G. B. Marin, and R. D. Gryse, *J. Electron Spectros. Relat. Phenomena*, **135**, 167 (2004).
22. G. Silversmit, D. Depla, H. Poelman, G. B. Marin, and R. De Gryse, *Sur. Sci.*, **600**, 3512 (2006).
23. J. Mendialdua, R. Casanova, Y. J. J. O. E. S. Barbaux, and R. Phenomena, *J. Electron Spectros. Relat. Phenomena*, **71**, 249 (1995).
24. A. Lipatov, M. Alhabeb, M. R. Lukatskaya, A. Boson, Y. Gogotsi, and A. Sinitskii, *Adv. Electron. Mater.*, **2**, 1600255 (2016).
25. Y. Li, J. Yao, E. Uchaker, J. Yang, Y. Huang, M. Zhang, and G. Cao, *Adv. Energy Mater.*, **3**, 1171 (2013).
26. J. Wang, J. Polleux, J. Lim, and B. Dunn, *J. Phys. Chem. C*, **111**, 14925 (2007).
27. T. C. Liu, *J. Electrochem. Soc.*, **145**, 1882 (1998).
28. Z. Tian, X. Tong, G. Sheng, Y. Shao, L. Yu, V. Tung, J. Sun, R. B. Kaner, and Z. Liu, *Nat. Commun.*, **10**, 4913 (2019).
29. Z.-l. Wang, D. Xu, L.-m. Wang, and X.-b. Zhang, *Chem. Plus. Chem*, **77**, 124 (2012).
30. X. Rui, Z. Lu, H. Yu, D. Yang, H. H. Hng, T. M. Lim, and Q. Yan, *Nanoscale*, **5**, 556 (2013).
31. J. Cheng, B. Wang, H. L. Xin, G. Yang, H. Cai, F. Nie, and H. Huang, *J. Mater. Chem. A*, **1**, 10814 (2013).
32. X. Wang, W. Jia, L. Wang, Y. Huang, Y. Guo, Y. Sun, D. Jia, W. Pang, Z. Guo, and X. Tang, *J. Mater. Chem. A*, **4**, 13907 (2016).
33. D. Zhu, H. Liu, L. Lv, Y. D. Yao, and W. Z. Yang, *Scr. Mater.*, **59**, 642 (2008).
34. Y. L. Cheah, V. Aravindan, and S. Madhavi, *ACS Appl. Mater. Interfaces*, **4**, 3270 (2012).
35. X. Rui et al., *RSC Adv.*, **1**, 117 (2011).
36. Y. Zhang, A. Pan, Y. Wang, W. Wei, Y. Su, J. Hu, G. Cao, and S. Liang, *ACS Appl. Mater. Interfaces*, **8**, 17303 (2016).
37. M. M. Rahman, A. Z. Sadek, I. Sultana, M. Srikanth, X. J. Dai, M. R. Field, D. G. McCulloch, S. B. Ponraj, and Y. Chen, *Nano Res.*, **8**, 3591 (2015).